



Supplementary Materials for

Amorphous TiO₂ Coatings Stabilize Si, GaAs, and GaP Photoanodes for Efficient Water Oxidation

Shu Hu, Matthew R. Shaner, Joseph A. Beardslee, Michael Lichterman, Bruce S. Brunshawig, Nathan S. Lewis*

*Corresponding author. E-mail: nslewis@caltech.edu

Published 30 May 2014, *Science* **344**, 1005 (2014)
DOI: 10.1126/science.1251428

This PDF file includes:

Materials and Methods
Supplementary Text
Figs. S1 to S17
References (32, 33)

Materials and Methods

Chemicals

All materials were used as received, except where otherwise noted. Sulfuric acid, concentrated hydrochloric acid and hydrogen peroxide were purchased from EMD Chemicals. H₂O with a resistivity of 18.2 MΩ·cm was obtained from a Millipore de-ionized water system.

An aqueous solution that contained the Fe(CN)₆^{3-/4-} redox couple was prepared by making a solution of 50 mM K₃Fe(CN)₆ (Fisher Scientific, 99.4%) and 350 mM K₄Fe(CN)₆ (Fisher Scientific, 99.4%) in 200 mL of H₂O. A 1.0 M aqueous solution of KOH (semiconductor grade, Sigma-Aldrich, 99.99% trace metal basis) was also prepared.

For non-aqueous electrochemistry, acetonitrile (CH₃CN, anhydrous, 99.8%, Sigma Aldrich) was dried by flowing through a solvent column, and then was stored over 3Å, activated, molecular sieves (Sigma-Aldrich). LiClO₄ (battery grade, 99.99%, Sigma Aldrich) was dried by fusing the salt under a pressure < 1×10⁻³ Torr at 300 °C. Prior to use, the resulting material was stored under ultra-high purity (UHP) Ar(g) that contained < 0.2 ppm of O₂(g). Bis(cyclopentadienyl) iron(II) (ferrocene, FeCp₂⁰) was purchased from Sigma Aldrich and was purified by sublimation under vacuum. Bis(cyclopentadienyl) iron(III) tetrakis(pentafluoroborate) (ferrocenium, FeCp₂⁺ • BF₄⁻) was purchased from Sigma Aldrich, recrystallized in a mixture of diethyl ether and acetonitrile (EMD Chemicals), and dried under vacuum prior to use. These reagents were used to prepare a solution that contained reagent concentrations of 1.0 M LiClO₄, 0.5 mM ferrocenium, and 90 mM ferrocene.

Preparation of Si, GaAs, and GaP substrates

Three types of Si wafers were used as substrates for atomic layer deposition: p⁺-Si (B-doped with a resistivity, $\rho < 0.002 \text{ } \Omega \cdot \text{cm}$, 3" diameter); n-Si (P-doped with $\rho = 2.06 - 2.18 \text{ } \Omega \cdot \text{cm}$, 3" diameter); and n⁺-Si (As-doped with $\rho < 0.002 \text{ } \Omega \cdot \text{cm}$, 3" diameter). The Si surfaces were first cleaned using an RCA SC-1 procedure that involved soaking the Si wafers in a 3:1 (by volume) solution of H₂SO₄ (conc., ~ 18.4 M) and H₂O₂ (conc., ~ 1 M) for 10 min, and then placing the samples for ~ 10 s in a 10% (by volume) aqueous solution of hydrofluoric acid (conc. 31.8 M). The Si samples were then etched using the RCA SC-2 procedure of soaking in a 5:1:1 (by volume) solution of H₂O, concentrated hydrochloric acid (11.1 M), and hydrogen peroxide (conc. ~ 1 M) for 10 min at 75 °C.

A p⁺-GaAs wafer oriented to expose the (111) B surface (Zn-doped, acceptor concentration of $1 \times 10^{19} \text{ cm}^{-3}$, 2 inch by AXT, Inc.) was also used as a substrate for atomic-layer deposition. The GaAs was placed for 15 s in a solution of 0.04% (by volume) Br₂ (Acros Organics) in methanol (CH₃OH, low water, J.T.Baker) and was then immersed in 1.0 M KOH (aqueous solution of potassium hydroxide pellets, semiconductor grade, 99.99% trace metals basis, Sigma-Aldrich) for 15 s. The GaAs samples were rinsed with copious amounts of deionized H₂O, and were then dried using a stream of N₂(g).

Prior to ALD, n-type GaP samples were etched, and ohmic contacts were formed, using a published procedure.⁽³²⁾ n-GaP samples were prepared from n-GaP wafers that had a sulfur dopant density of $\sim 5 \times 10^{17} \text{ cm}^{-3}$. Small ($\sim 0.3 \text{ cm}^2$) pieces were cut from the

wafer using a scribe, and the pieces were then etched in 18.4 M H₂SO₄ for 30 s, followed by a rinse with copious amount of de-ionized H₂O.

Fabrication of planar np⁺-Si and np⁺-GaAs samples

A 4" n-Si (0.1-0.3 ohm-cm, <100> oriented, single-side polished) wafer was cleaned prior to formation of the p⁺ emitter. The cleaning procedure consisted of a 30 s in Buffered hydrofluoric acid (BHF) etch (Transene, Inc.); 20 min in an RCA I (5:1:1 of H₂O:H₂O₂:NH₄OH) organic-species cleaning solution at 70 °C; a BHF etch for 30 s; and 20 min RCA II (6:1:1 of H₂O:HCl:H₂O₂) metals cleaning at 70 °C, with water rinses between each process step. Immediately following this cleaning procedure, the wafer was cleaved into ~1" × 1" pieces, to fit into the doping furnace. Each piece was then etched for 30 s in BHF, rinsed with H₂O, dried with N₂(g), and loaded into a boron-doping furnace. Wafer pieces were loaded back-to-back on a quartz boat with the polished side facing out, and were placed between Saint Gobain BN-975 boron-doping wafers that over-filled each n-Si piece. For each doping run, six 1" × 1" n-Si pieces were loaded into 3 slots. Each doping run was performed in a 4" tube furnace at 950 °C under a 10 L min⁻¹ flow of N₂(g). In each run, the boat was loaded into the tube furnace during a 1 min period, and was then soaking at 950 °C for 3 min and unloaded over another 1 min period. Following two doping runs (12 total samples), each sample was etched for 30 s in BHF and then was loaded, without a dopant source, into the doping furnace with a 5 L min⁻¹ flow of O₂(g) for 30 min at 750 °C, to grow a low temperature oxide (LTO). This LTO allowed facile removal of residual boron on the surface through a 30 s BHF etch.

Planar np⁺-GaAs junctions were grown epitaxially on an n⁺-GaAs wafer that had a (100)-oriented, polished surface (Si-doped, donor concentration of 1×10¹⁸ cm⁻³, 2 inch by MTI, Inc.). A 2 μm thick n-GaAs layer (Si-doped, donor concentration of 2×10¹⁷ cm⁻³) and a 100 nm thick p⁺-GaAs layer (Si-doped, acceptor concentration of ~5×10¹⁸ cm⁻³) were sequentially grown on the n⁺-GaAs substrate. The edges of both the np⁺-Si and np⁺-GaAs wafers were cleaved off and discarded, to eliminate shunts from the back side of the sample to the front p⁺ emitter.

Atomic layer deposition of TiO₂

TiO₂ films were deposited onto Si, GaAs, and GaP substrates at 150 °C using a Cambridge Nanotech S200 ALD system. The Si, GaAs, and GaP surfaces were prepared as described above and loaded immediately thereafter into the ALD chamber. Each ALD cycle consisted of a 0.015 s pulse of H₂O, followed by a 0.10 s pulse of tetrakis-dimethylamidotitanium (TDMAT, Sigma-Aldrich, 99.999%, used as received). A 15-s purge under a constant 0.02-L min⁻¹ flow of research-grade N₂(g) was performed between each precursor pulse. When idle, the ALD system was maintained under a continuous N₂(g) purge and had a background pressure of 2.7×10⁻¹ Torr.

Deposition of metal films and fabrication of island patterns

Both electron-beam evaporation and radio-frequency sputtering were used to deposit Ni onto patterned and unpatterned TiO₂ surfaces. The electrochemical performance was essentially identical for both sputtered and e-beam evaporated Ni. The as-deposited Ni films were 100 nm thick for p⁺-Si and p⁺-GaAs in Fig. 1 and 4, were nominally 2 nm

thick for n-GaP and np⁺-GaAs in Fig. 1, and were nominally 3 nm thick for the XPS study in Fig. S17. The deposition rate was calibrated using profilometry. 100-nm thick Ni films were also deposited on flat quartz slides as a control sample in Fig. 1 and 4.

A series of photolithography, physical vapor deposition, and lift-off steps was used to fabricate Ni-island patterns on TiO₂ overlayers that had been grown on n-Si, np⁺-Si and np⁺-GaAs substrates. The mask used for the island pattern was a square array of 3 μm-diameter circles with a 7-μm pitch. Ni islands (100 nm thick) on TiO₂ were fabricated by lifting off positive photoresist films, S1813 (Shipley), which were patterned to mask deposited Ni layers. The photoresist was removed using PG remover (MicroChem) followed by rinsing the surface of the sample with copious amount of H₂O.

Optical absorbance measurements

The optical absorbance of the n-Si/TiO₂/Ni-island samples was determined by integrating sphere transmission (*T*) and reflection measurements for both sides of the samples (*R*₁ and *R*₂) at normal incidence. For transmission measurements, the sample was mounted at the front port of the integrating sphere, whereas for reflection measurements the sample was mounted at the rear port of the sphere. The optical reflection was normalized to a reflectance standard (99%, LabSphere, Inc) that was placed at the same location as the sample. The absorbance (as a function of wavelength, λ) was determined from the measured reflection and transmission, assuming sufficient absorption of the sample, as follows:

$$A(\lambda) = 1 - R_1(\lambda) - \frac{T(\lambda)}{1 - R_2(\lambda)}$$

Electrode preparation

Ohmic contacts to the semiconducting electrodes were formed by rubbing an In-Ga eutectic onto the unpolished back sides of the Si samples; by sequentially depositing Ni/Cu films onto the unpolished back sides of the p⁺-GaAs samples; or by soldering In to the back side of n- p⁺-GaAs or n-GaP samples. The np⁺-GaAs samples were then annealed under forming gas at 450 °C for 30 s whereas the n-GaP samples were annealed under forming gas at 400 °C for 10 min. For aqueous electrochemistry, Ag paste was used to attach the samples to a piece of Cu tape as a current collector. The sample assembly was then assembled into a custom-made Teflon compression cell equipped with an O-ring seal (0.0314 cm² in electrode area). For electrochemistry using glass-rod electrodes, Ag paste was used to attach the ohmic contact on the back side of the samples to a coiled, tin-plated Cu wire which was then threaded through a glass tube. The sample was then encapsulated and sealed to the glass tube using grey epoxy (Hysol 9460F). An optical scanner was used to image the exposed electrode surface areas and the areas were measured using ImageJ software. All the electrodes in this study were typically 0.2 – 1.3 cm² in area.

Aqueous and non-aqueous electrochemical measurements

A saturated calomel electrode (SCE, CH Instruments) was used as a reference electrode for electrochemical measurements that were performed using aqueous solutions, including photoelectrochemical, spectral response and faradaic efficiency measurements. Pt gauze (100 mesh, 99.9% trace metal basis, Alfa-Aesar), was used as

the counter electrode during electrochemical measurements with the $\text{Fe}(\text{CN})_6^{3-/4-}$ couple, and a carbon rod placed within a fritted glass tube (Aceglass, Inc.) was used as the counter electrode for 1.0 M KOH(aq) solution. A carbon counter electrode in a fritted glass tube eliminated the possibility of contamination of the electrolyte and thus the working photoelectrode by trace Pt that would result from minute dissolution of the material in a Pt counter electrode. The formal potential for the oxidation of H_2O to O_2 (g), 0.19 V vs. SCE, was calculated from the measured pH of the solution (pH 13.7) and using SCE = 0.24 V vs. NHE. Consistently, the open-circuit potential of a Ni film electrode in 1.0 M KOH was measured as 0.19 V vs. SCE. The Nernstian potential of the 50 mM $\text{Fe}(\text{CN})_6^{3-}$ and 350 mM $\text{Fe}(\text{CN})_6^{4-}$ (aq) solution was 0.19 V vs. SCE, as obtained by measuring the potential difference of a 2 mm-diameter Pt disc vs. an SCE in the solution, and the open-circuit voltage was determined as the potential difference at open-circuit under illumination between the photoelectrode and a counterelectrode poised at the Nernstian potential of the electrolyte solution.

A Pt wire (0.5 mm diameter, 99.99% trace metals basis, Alfa-Aesar) was used as a reference electrode and a Pt gauze was used as the counter electrode for electrochemical measurements made in the non-aqueous solutions. A custom electrochemical cell with a Pyrex flat bottom was used for non-aqueous electrochemistry. During measurements, the electrolyte was rigorously agitated with a magnetic stir bar driven by a model-train motor. All of the data presented for electrochemical measurements in aqueous solutions included compensation for the series resistance of the solution, as obtained from high-frequency electrical-impedance measurements.

A Xe lamp-based solar simulator, as well as ELH-type and ENH-type tungsten-halogen lamps, were used for photoelectrochemical experiments. The illumination intensity was calibrated by placing a Si photodiode (Thor Labs) in the glass electrochemical cell or in a Teflon compression cell, in the same location that was occupied by the exposed area of a photoelectrode. The Si photodiode was previously calibrated by measurement of the short-circuit current-density value under AM 1.5 simulated sunlight at 1-Sun, i.e., at 100 mW cm^{-2} of irradiance from a Xe arc lamp with an AM 1.5 filter.

Oxygen-evolution efficiency measurements

A Neofix fluorescence probe was used in an airtight cell with a side-facing quartz window. The oxygen concentration was monitored throughout the measurement, and was tabulated via measured values from a fluorescence detector. These values were calibrated using the standard concentration of oxygen in water ($7700 \mu\text{g L}^{-1}$ or 2.4×10^{-4} M) under a standard 20.9% (by volume) oxygen atmosphere. A Ag/AgCl electrode was the reference electrode, and the counter electrode was a carbon rod that was positioned in a separate, fritted compartment. The cell volume was 52 mL, and the cell was purged with a stream of UHP Ar(g) for ~1.5 h prior to data collection. The experiment lasted for 30 min after a 10-min waiting period at open circuit. The oxygen concentration was monitored throughout the measurement.

The data were collected and modeled using a Matlab script. The oxygen concentration data were converted into micrograms of O_2 by first correcting for the O_2 leak rate measured during the first 10 min of the experiment, followed by calculating the mass of O_2 in micrograms at each time point. The calculation process was performed by

multiplying the reported percentage of oxygen by the number of micrograms of O₂ dissolved in water at room temperature under 1 atm, 7700 µg L⁻¹ (assuming the value the same as in 1.0 M aqueous acidic solutions), and the cell volume (52 mL), divided by the concentration of O₂ in air under 1 atm, which was in the value reported by the fluorescence probe (20.9%). To compare the charge versus time data from the potentiostat with the amount of oxygen generated versus time, 100% Faradaic efficiency was assumed for comparison. Specifically, the amount of charge passed (in mA·h) was multiplied by 3.6 to convert the data into coulombs; this value was then multiplied by 83 to convert the value into micrograms of O₂, because this is the conversion factor of 1 coulomb of electrons into 1 microgram of O₂. Therefore, both the cumulative oxygen generated and charge passed during the measurement can be shown in one plot with two comparable y axes, where 0.33 mA·h of charge passed corresponded to 100 µg O₂ generated. The electrode area for the measured Si, GaAs and GaP photoanodes are 0.26, 0.20 and 0.47 cm², respectively.

Secondary-ion mass spectrometry (SIMS)

Secondary-ion mass spectrometry (SIMS) analysis was performed using a Cameca SIMS-7f GEO instrument. A Cs⁺ primary ion beam was used to ionize and sputter surface atoms from the sample. The sputtered, ionized atoms (secondary ions) were collected and analyzed in a mass spectrometer. The samples were sputtered at normal incidence with a 7 keV Cs⁺ beam at substrate bias of 4 keV. The raster area was 125 µm × 125 µm, with a centered 12500 µm² gated area. Count rates of ³⁰Si, ⁴⁸Ti, ¹²C + ¹³³Cs and ¹⁴N + ¹³³Cs (complex ions) were recorded as a function of sputtering time.

Spectroscopic ellipsometry

Complex refractive index (*n*, *k*) data for films of unannealed, as-grown TiO₂ on n⁺-Si were obtained using spectroscopic ellipsometry. The ellipsometric data were acquired using a J.A. Woolam V-VASE system. The non-absorbing (*k*~0) portion of the data were fit using a Cauchy model that assumed a TiO₂/SiO₂ bilayer structure on Si. The TiO₂ *n*, *k* values were extracted from a point-by-point fit, using fixed Cauchy and film-thickness parameters. Measurements were performed on TiO₂ films with thicknesses of 4 nm, 31 nm, 44 nm, 68 nm, and 143 nm, with the extracted *n*, *k* values being comparable for all film thicknesses.

Electron microscopy

Transmission electron microscopy (TEM) was performed using a JOEL JEM-2100F operating at an accelerating voltage of 200 kV. The bright-field images and selected-area electron diffraction patterns were acquired under TEM mode, while the elemental-contrast images (Fig. 3A) and energy-dispersive x-ray spectroscopy data (Fig. 3B) were acquired under scanning TEM mode. The cross-sectional TEM sample was polished to 5 µm in thickness using a series of diamond lapping films, and the samples were then further polished to 50 – 100 nm thin foils by a Gatan precision ion polishing system.

X-ray photoelectron spectroscopy

X-ray photoelectron spectroscopy (XPS) was performed using a Kratos Axis Ultra system with a base pressure of < 1×10⁻⁹ Torr. A monochromatic Al Kα source was used

to illuminate the sample with 1486.7 eV photons at a power of 150 W. A hemispherical analyzer oriented for detection along the sample surface normal was used for maximum depth sensitivity. Survey scans were obtained at a resolution of 1 eV with a pass energy of 80 eV. Detailed scans were acquired at a resolution of 25 meV with a pass energy of 10 eV, using variable acquisition times. When cleaning of adventitious species such as C was required, an octopole ion gun was used to sputter-clean the sample surface with 500 eV Ar ions for 30 – 60 s. ~10 min of air exposure occurred between sample transfers from the ALD or sputtering deposition tool to the XPS load lock.

Measurement of charged-carrier density (Hall measurements)

TiO₂ films were grown on glass slides by the aforementioned ALD procedure. The glass slides were cleaned by sequential rinsing with acetone, isopropanol and ethanol for 1 min each. The samples used for Hall measurements were made by cutting TiO₂-coated glass into 1 cm × 1 cm square pieces, and In was directly soldered onto the four corners of the TiO₂ film. The current-supply leads and voltage probes were connected to the Hall measurement circuit board through In-soldered Cu wires. Ohmic conduction was confirmed by current-voltage (*I-V*) measurements of any two of the four In-contacted corners, with the supplied current in the range of 50 – 100 nA. The magnetic field was fixed at 3000 gauss. TiO₂ films having thicknesses of 4 nm, 31 nm, 44 nm, 68 nm, and 143 nm were measured, and all showed n-type conduction with an average electron concentration of $4 \times 10^{16} \text{ cm}^{-3}$.

Hg droplet measurements

A Hg droplet was placed on ALD TiO₂-coated Si samples, with the contact area confined by a 2 mm diameter O-ring. A Pt wire was inserted into the Hg droplet to make the top contact, whereas the ohmic bottom contact was formed by rubbing In-Ga eutectic into the unpolished back side of the Si. The bias polarity was kept the same as in the electrochemical measurements of Fig. 1 and 4, i.e. positive voltage corresponded to a forward bias of the p⁺-Si substrate with respect to a Hg droplet, and positive current corresponded to anodic currents in which holes flowed from the Si to the Hg droplet.

Mott-Schottky analysis

The Mott-Schottky analysis (Fig. S15) of the area-corrected differential capacitance–potential data was obtained using electrochemical impedance spectroscopy.⁽³¹⁾ The solution was quiescent and kept in dark during the measurements. The electrochemical impedance data were fit to a model that consisted of a parallel resistor and capacitor with a fixed constant phase element arranged electrically in series with a separate resistor.

Supplementary Text

Load-line analysis

The *J-E* behavior of a serially connected Si PV cell and an electrocatalytic anode was calculated by negatively shifting the *J-E* characteristic of the electrolytic anode by the photovoltage of the PV cell at each photocurrent density. The photocurrent density (*J*) – voltage (*V*) performance of the ideal Si PV cell was calculated using the ideal diode equation: $J = J_L - J_0(e^{\frac{qV}{kT}} - 1)$, where *J_L* is light-limited current density (*J_L*=27.7

$\text{mA}\cdot\text{cm}^{-2}$), J_0 is dark current density, q is the unsigned charge on the electron, k is Boltzmann's constant, and T is the absolute temperature ($T = 300\text{ K}$). Obtaining a V_{oc} of the ideal Si cell that reproduced the observed 0.32% thermodynamic water-oxidation efficiency required a value of $J_0 = 1.55 \times 10^{-6}\text{ mA}\cdot\text{cm}^{-2}$ for the PV cell component of the series-connected system used in the model. An analogous procedure for GaAs-based systems required a PV cell having a $J_0 = 1.25 \times 10^{-12}\text{ mA}\cdot\text{cm}^{-2}$, which produced a $V_{oc} = 0.77\text{ V}$, in combination with a $J_L = 14.3\text{ mA}\cdot\text{cm}^{-2}$ and a fill factor of 0.86 and a PV energy-conversion efficiency of 9.5%, in series with a $\text{p}^+\text{-GaAs}/\text{TiO}_2/\text{Ni}$ -film dark electrode (Fig. S2B), to produce the J - E behavior observed for the $\text{n-p}^+\text{-GaAs}/\text{TiO}_2/\text{Ni}$ -film integrated photoelectrode system (Fig. 1D). If a 25% absorption loss of Ni catalysts is considered, a 12.7% GaAs PV cell would be required, and the water-oxidation efficiency would be 6.6% at a light-limited photocurrent density of $19.1\text{ mA}\cdot\text{cm}^{-2}$ when there's negligible optical absorption loss.

ALD growth rate

ALD samples with 250, 750, 1000 and 1500 and 3000 cycles of pulsed precursors were grown on p^+ and n^+ Si substrates. These growths produced film thicknesses of 4.3 nm, 30.7 nm, 43.5 nm, 68.3 nm and 142.5 nm, corresponding to a growth rate of $\sim 0.5\text{ \AA}/\text{cycle}$. The ellipsometrically measured and fitted film thicknesses agreed with the thicknesses obtained from TEM micrographs (Fig. S7).

Energy-conversion properties of photoelectrodes

A bare $\text{n-p}^+\text{-Si}$ electrode in contact with a non-aqueous electrolyte that contained 0.5 mM ferrocenium and 90 mM ferrocene (Fc) with 1.0 M LiClO_4 dissolved in dry CH_3CN exhibited $V_{oc} = 0.50 - 0.55\text{ V}$, a short-circuit current density, J_{sc} , of $33.6 \pm 5.0\text{ mA}\cdot\text{cm}^{-2}$, and a fill factor, ff , of 0.29, with a photoelectrode energy-conversion efficiency of 5.42% under simulated 1-Sun illumination (Fig. S3). The V_{oc} of the $\text{n-p}^+\text{-Si}$ junction was therefore within experimental error of the photovoltages exhibited by the $\text{n-p}^+\text{-Si}/\text{TiO}_2/\text{Ni}$ -island electrodes. The presence of the thick TiO_2 film thus resulted in $< 50\text{ mV}$ voltage losses for both minority- and majority-carrier hole conduction. In contrast to the behavior shown in Fig. 1B, a photovoltage of $< 5\text{ mV}$ was observed when Ni islands were directly deposited and patterned onto n-Si electrodes (Fig. S4), presumably due to the formation of nickel silicide at the Si/Ni interface. In addition to producing negligible photovoltages under alkaline anodic operating conditions, the Ni on the $\text{n-Si}/\text{Ni}$ samples was undercut and the underlying Si was etched consequently, in accord with prior observations (14) and with expectations based on the chemical and photoanodic instability of unprotected or poorly protected Si electrodes in alkaline media.

Description of XPS data

Fig. S17 shows the X-ray photoelectron spectra for the Ti 2p and Ni 2p core-levels for a 3-nm Ni film deposited on ALD-grown TiO_2 . The chemical shift of the Ti 2p_{1/2} and Ti 2p_{3/2} peaks indicates that only the Ti^{4+} chemical states were present in the as-grown TiO_2 . The interfacial Ni may be present in various oxidation states, with Ni_2O_3 and nickel oxide hydroxide (when present) contributing to the peak at 855.9 eV binding energy. At the Ni/ TiO_2 interface, the oxidation state of Ti remained Ti^{4+} as compared

with ALD-grown TiO₂, because the binding energy of the Ti 2p XPS core-level spectra remained at 459.0 eV after Ni deposition.

The valence-band offset of TiO₂ relative to the Si substrate was determined by XPS using the Kraut method, as described by Wallrapp *et al.* (33). High-resolution scans were obtained from the Fermi edge to the Si 2p and Ti 3p peaks, for Si that was cleaned by the RCA SC-2 procedure as well as for a bulk film of TiO₂ deposited via ALD. The valence-band maximum (VBM) for the RCA SC-2 cleaned Si and for the 43.5 nm TiO₂ film on Si was determined by a linear extrapolation of the Fermi edge to the binding energy axis (Fig. S13A and S13C). The differences between the intensity maxima of the Si 2p and Ti 3p core-level peaks and their corresponding valence-band maxima, respectively, were taken as the energy of the core level orbitals, which were found to be 98.86±0.005 eV and 34.36±0.02 eV, respectively. A high-resolution scan of a Si substrate with a thin TiO₂ layer (190 cycles of ALD on Si) was acquired over an energy range that spanned the Si 2p peak and the Ti 3p peak (Fig. S13B). The core level offset (of 62.30 ± 0.06 eV) between the Si 2p and Ti 3p signals was determined by the difference in energy values between the intensity maxima of the two peaks. The overall valence-band offset across the Si/TiO₂ interface was then calculated as the difference between the Si 2p to VBM value and the Ti 3p to VBM value, subtracted from the offset between the Si 2p and Ti 3p peaks. The VB offset value was determined to be 2.22 ± 0.08 eV for ALD-grown TiO₂ films on Si with interfacial layers prepared by the RCA SC-2 etching procedure.

Description of optical absorption data

Tauc plots (Fig. S14) were generated by plotting $(\alpha h\nu n)^{1/2}$ as a function photon energy, where α is the absorption coefficient ($\alpha = 4\pi k / \lambda$), and k is Planck's constant. The two small peaks observed in the Tauc plot were consistent with the presence of defect bands in the unannealed, as-grown TiO₂ films. The optical band gap of the as-grown TiO₂, 3.34 ± 0.01 eV, was determined by a linear extrapolation of the optical absorption edge in the Tauc plot to the y axis.

Ir overlayers on TiO₂

Ir was selected as an alternative metal to evaluate the generality of the TiO₂/electrocatalyst structure relative to TiO₂/Ni. Ir has a higher work function (5.3 – 5.7 V) than Ni (4.8 – 5.0 V) as measured in vacuum. RuO_x has limited stability under acidic and basic conditions. IrO_x is considered as a stable OER catalyst in base, and only IrRuO_x catalysts, used in dimensionally stable anodes, are long-term stable in acid. In base, although RuO_x is more active than IrO_x, RuO_x is not significantly more active than Ni-based OER catalysts: for example, McCrory *et al.* (29) recently showed that IrO_x has an overpotential of 330 mV as compared to NiFeO_x of 360 mV when both produce anodic current densities of 10 mA·cm⁻² for the OER.

Long-term stability of photoelectrodes

An n-Si/TiO₂/Ni photoelectrode has run for >200 hours cumulatively, and the film did not prevent hole conduction, however longer term studies would be required to assess the very long term thermal stability of the film towards oxidation. Additionally, separate studies are needed to establish the efficacy of the unannealed film over very large

electrode areas to understand the defect density and defect tolerance of the electrodes in a manufacturing environment.

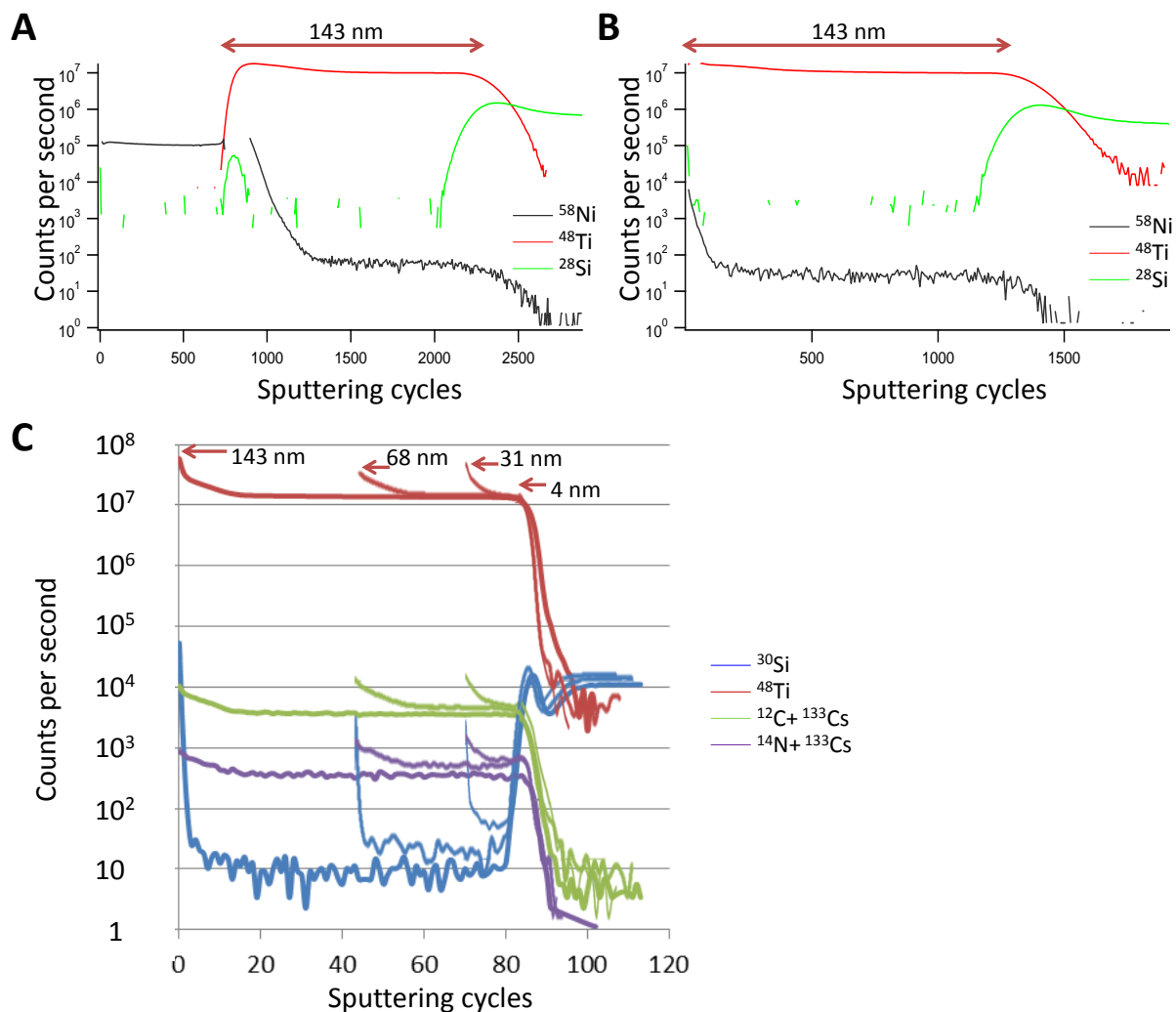


Fig. S1.

Secondary-ion mass spectrometry data of TiO_2 films on Si with Ni overlayers (a) and without Ni overlayers (b) of nominally 100 nm Ni thickness deposited by sputtering. The thickness of the TiO_2 films in (a) and (b) was 143 nm. If Ni had percolated through the TiO_2 films, the Ni signal in (a) would be above the background Ni concentration, as shown in (b). (c) C and N impurity profiles in ALD- TiO_2 films of 4 nm, 31 nm, 44 nm, and 143 nm in thickness. The C and N impurity levels were constant with depth throughout the films of various thicknesses, and were comparable to each other for various thicknesses.

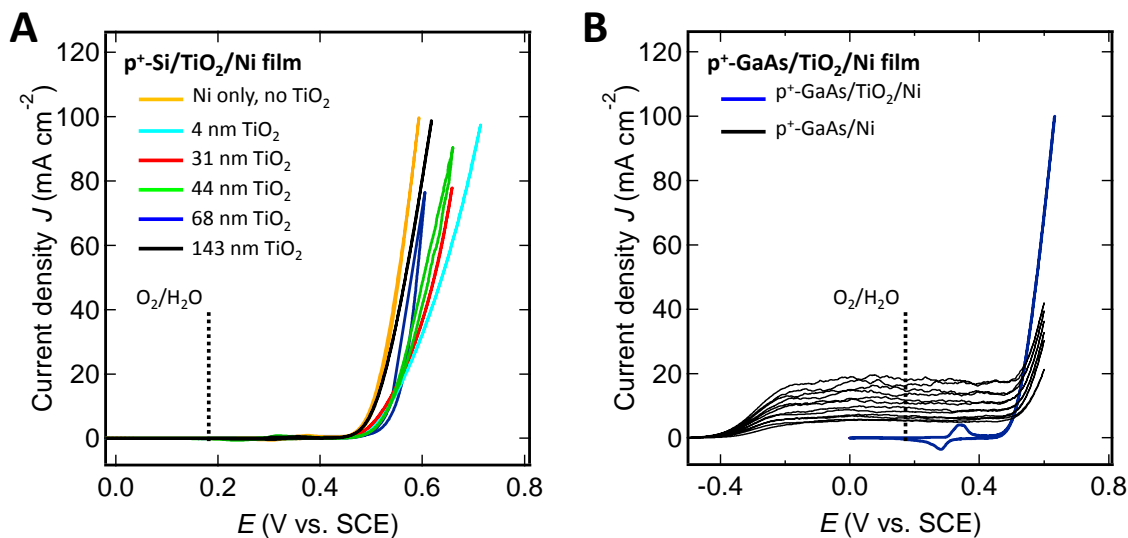


Fig. S2.

Dark J - E behavior of TiO_2 -coated $p^+\text{-Si}$ (a) and $p^+\text{-GaAs}$ (b) electrodes, covered with 100 nm Ni films, in contact with 1.0 KOH (aq). The cyclic-voltammetry data in both (a) and (b) were measured in the dark, and have been compensated for the ohmic series resistance of the electrolyte. The formal potential for water oxidation is labeled at 0.19 V vs. SCE. (a) 4 – 143 nm thick TiO_2 , as well as a 100 nm thick, continuous Ni film on quartz, as a control; and (b) is the same structure on $p^+\text{-GaAs}$ but with a TiO_2 thickness of 68 nm. The black curve in (b) shows increasing corrosion current for a $p^+\text{-GaAs}$ electrode without the TiO_2 overlayer present. The electrode area was typically 0.2 – 1.3 cm^2 .

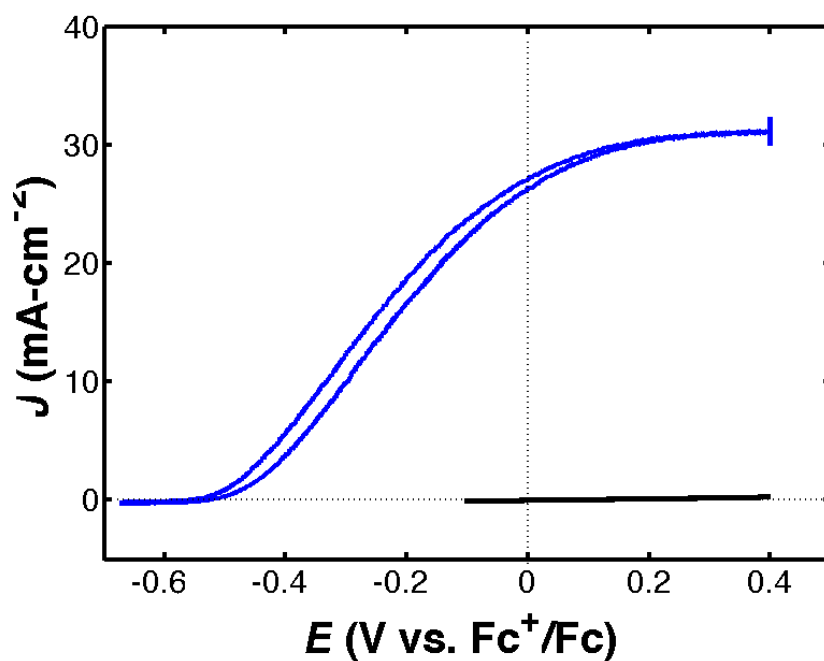


Fig. S3.

J-E behavior of an np^+ -Si buried junction (photoactive) in contact with 0.5 mM ferrocenium and 90 mM ferrocene (Fc) and 1.0 M LiClO_4 in CH_3CN , under simulated ELH-type 1-Sun illumination (blue curve) and in dark (black curve). The top p^+ -Si layer formed an ohmic contact to the $\text{Fc}^{+/0}$ redox couple.

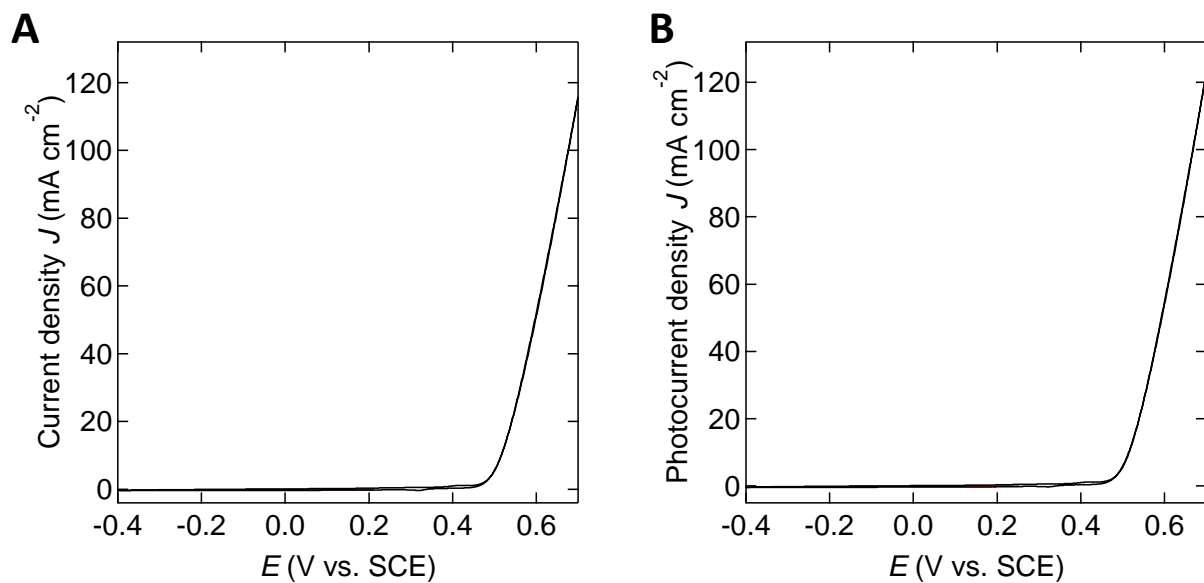


Fig. S4.

J - E behavior of Ni islands (100 nm thick, 3 μ m circles in 7 μ m pitch) on n-Si in 1.0 M KOH(aq), in the dark (A) and under illumination (B).

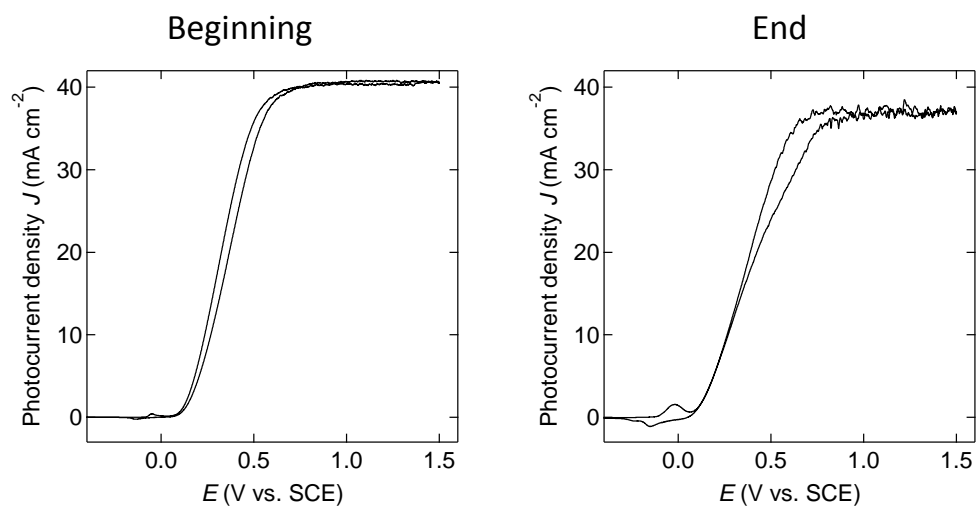


Fig. S5.

J - E data of an np^+ -Si photoelectrode coated with TiO_2 and Ni islands at various stages of chronoamperometry shown in Figure 3. The fill factors at each stage barely decreased, and the light-limited photocurrent density varied linearly with the illumination intensity.

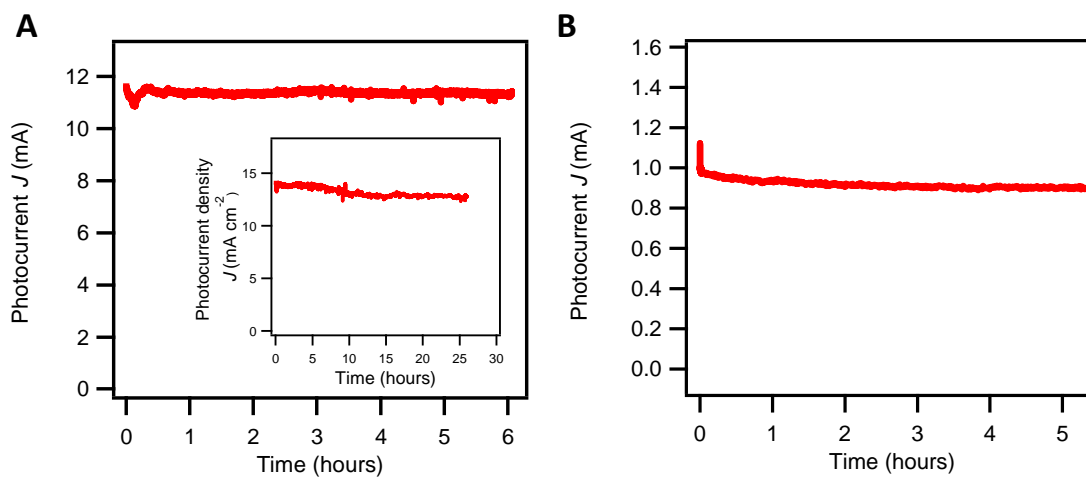


Fig. S6.

Photocurrent vs. time data, under simulated 1-Sun illumination at the formal potential for water oxidation (0.19 V vs. SCE), of a 2-nm Ni/118 nm TiO_2 -coated np^+ -GaAs photoanode (A) and a 2-nm Ni/118 nm TiO_2 -coated n-GaP (B) photoanode in 1.0 M KOH (aq) under constant simulated AM 1.5 1-Sun illumination. Stable photocurrents for > 25 hours are shown in the inset of (A). The GaAs and GaP electrode area was 0.82 cm^2 and 0.40 cm^2 , respectively.

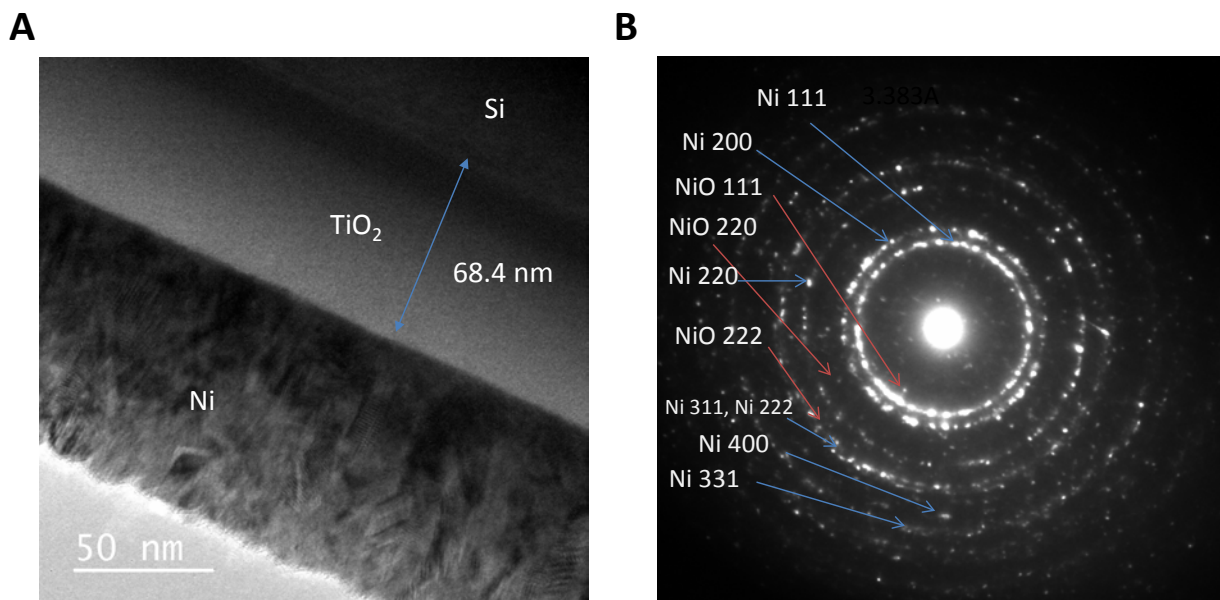


Fig. S7.

Cross-section TEM characterization of the Ni/ TiO₂/p⁺-Si interface. (A) Bright-field micrograph showing that the TiO₂ film thickness was measured to be 68.4 ± 0.8 nm. (B) Selective-area diffraction pattern at the Ni/TiO₂ interface.

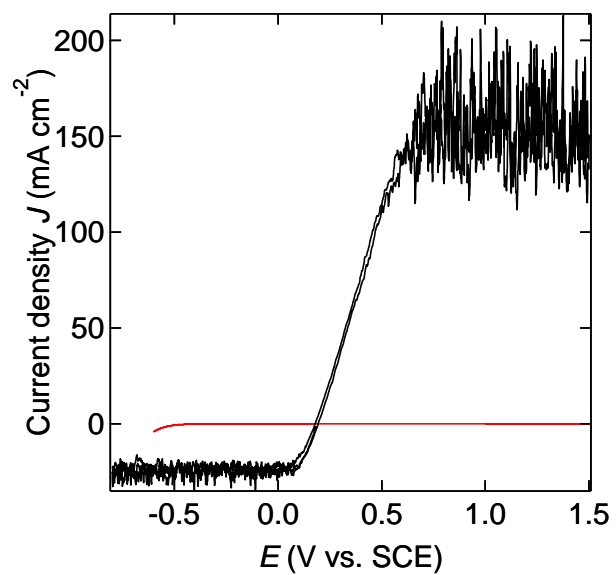


Fig. S8.

Dark J - E behavior of a nominally 100 nm Ni film on a 68 nm thick ALD-TiO₂ film on p⁺-GaAs (black curve) and bare 68 nm ALD TiO₂/p⁺-GaAs (red curve) in contact with 50 mM of K₃Fe(CN)₆ and 350 mM of K₄Fe(CN)₆ in H₂O.

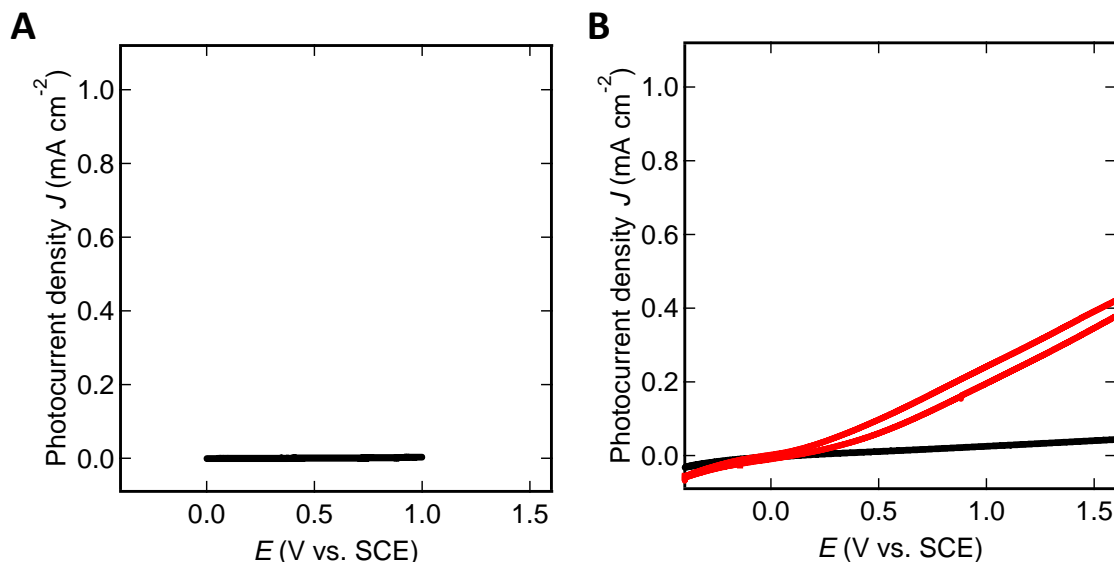


Fig. S9.

J-E data for 68 nm of ALD-TiO₂ on Si in contact with 1.0 M KOH (aq). (A) 68 nm TiO₂ on p⁺-Si in the dark exhibited negligible hole conduction through bare TiO₂ in 1.0 M KOH(aq). (B) 68 nm TiO₂ on n-Si in the dark (black curve) vs. under illumination (red curve) showed negligible photoactivity. The bare TiO₂ on n-Si sustained ~400 μA·cm⁻² of anodic current density, but this value is negligible when compared to the conductance behavior of the Ni/TiO₂/n-Si samples. This observation was general for all of the other thicknesses of TiO₂ films investigated, i.e., 4 nm, 31 nm, 44 nm, and 143 nm.

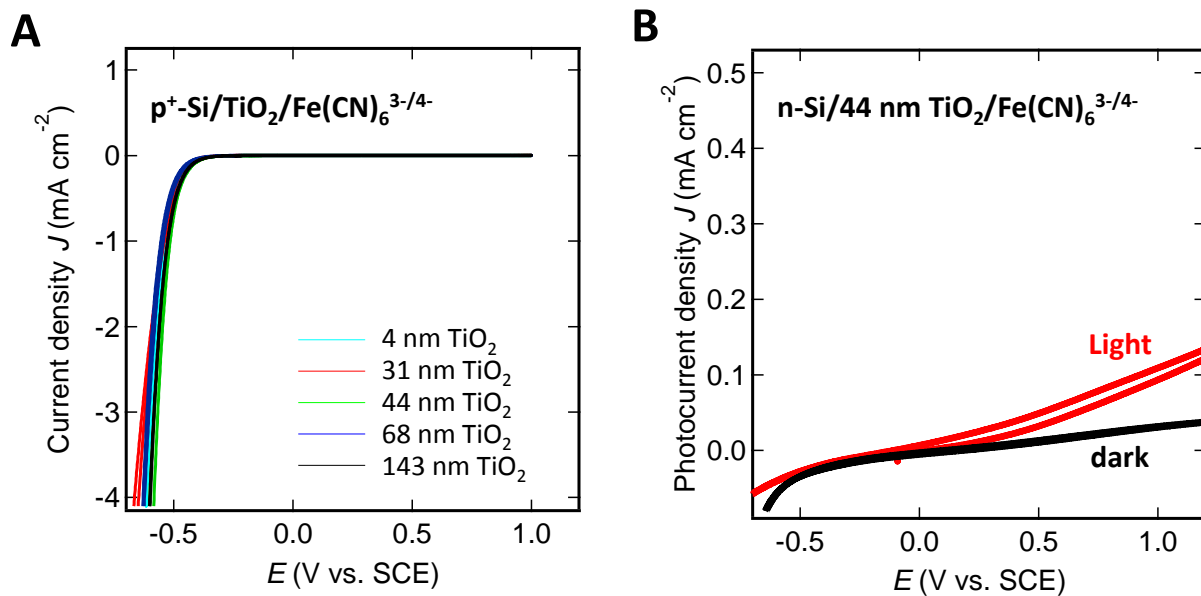


Fig. S10.

Electrochemical and photoelectrochemical behavior of bare ALD- TiO_2 coated Si without a Ni overlayer. (A) Bare ALD- TiO_2 on p^+ -Si in contact with 50 mM $K_3Fe(CN)_6$ and 350 mM $K_2Fe(CN)_6$ (aq) in the dark. (B) Bare ALD- TiO_2 on p^+ -Si in the same electrolyte under simulated ELH-type 1.25-Sun illumination.

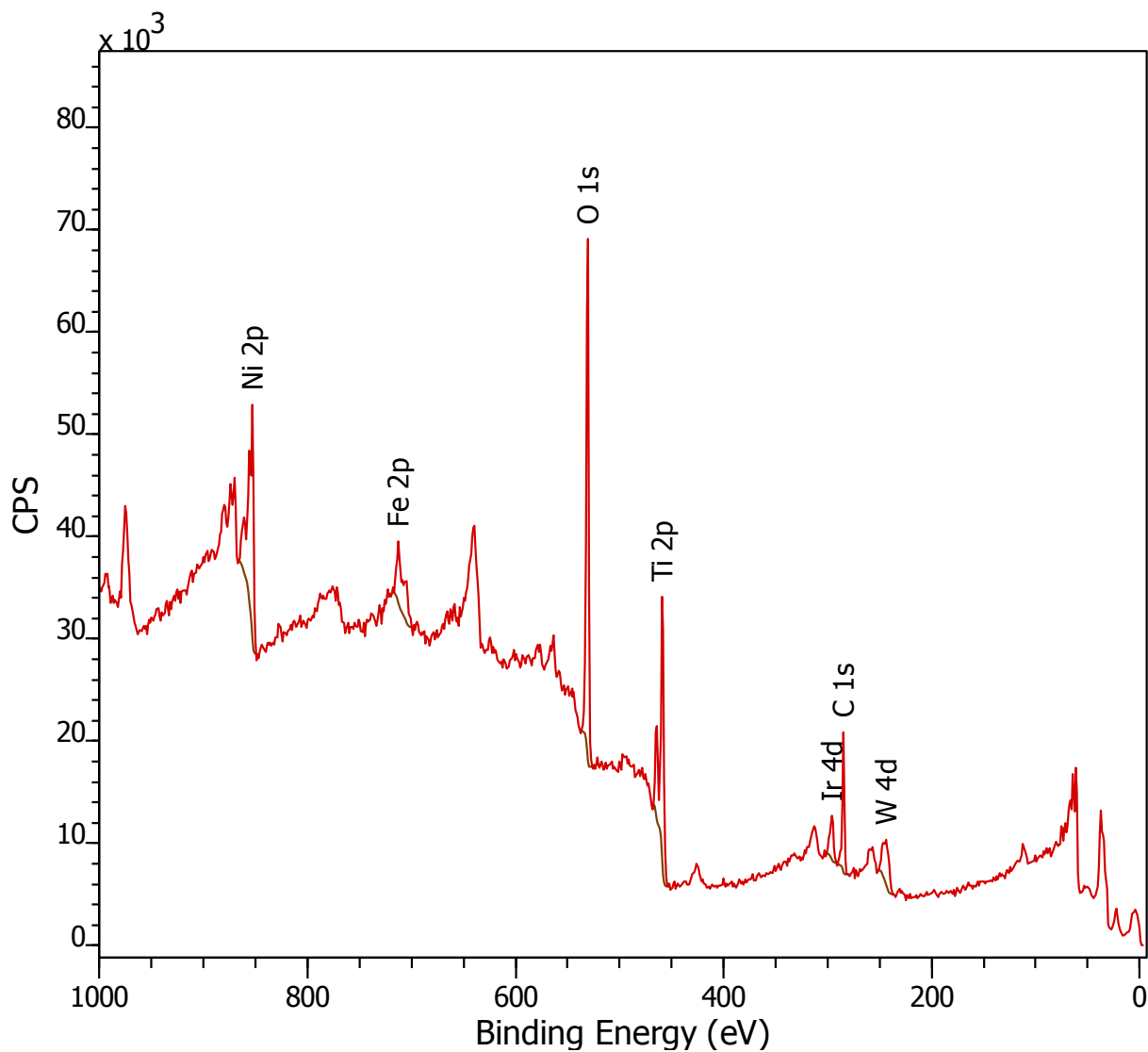


Fig. S11.

X-ray photoelectron spectroscopy survey scan of the surface of a TiO_2 overlayer on Si after an Ar-plasma sputtering treatment. Traces of Ni, Ir, Fe and W were present on the surface. The atomic compositions for O, C Ni, Ti, W, Ir and Fe were 45.5%, 31.2%, 5.1%, 12.7%, 1.9%, 0.9% and 2.8%, respectively.

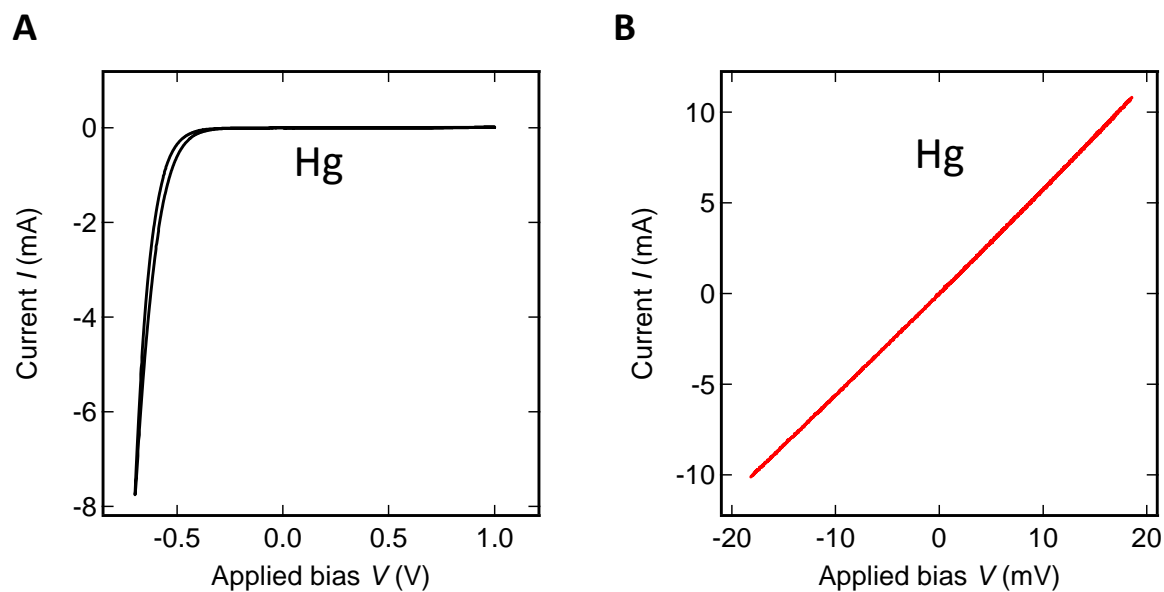


Fig. S12.

Current-voltage measurements of 68 nm ALD-TiO₂ on p⁺-Si using a mercury (Hg) droplet as the top contact, without (A) and with (B) etching of an insulating barrier layer at the surface of the ALD-TiO₂ film.

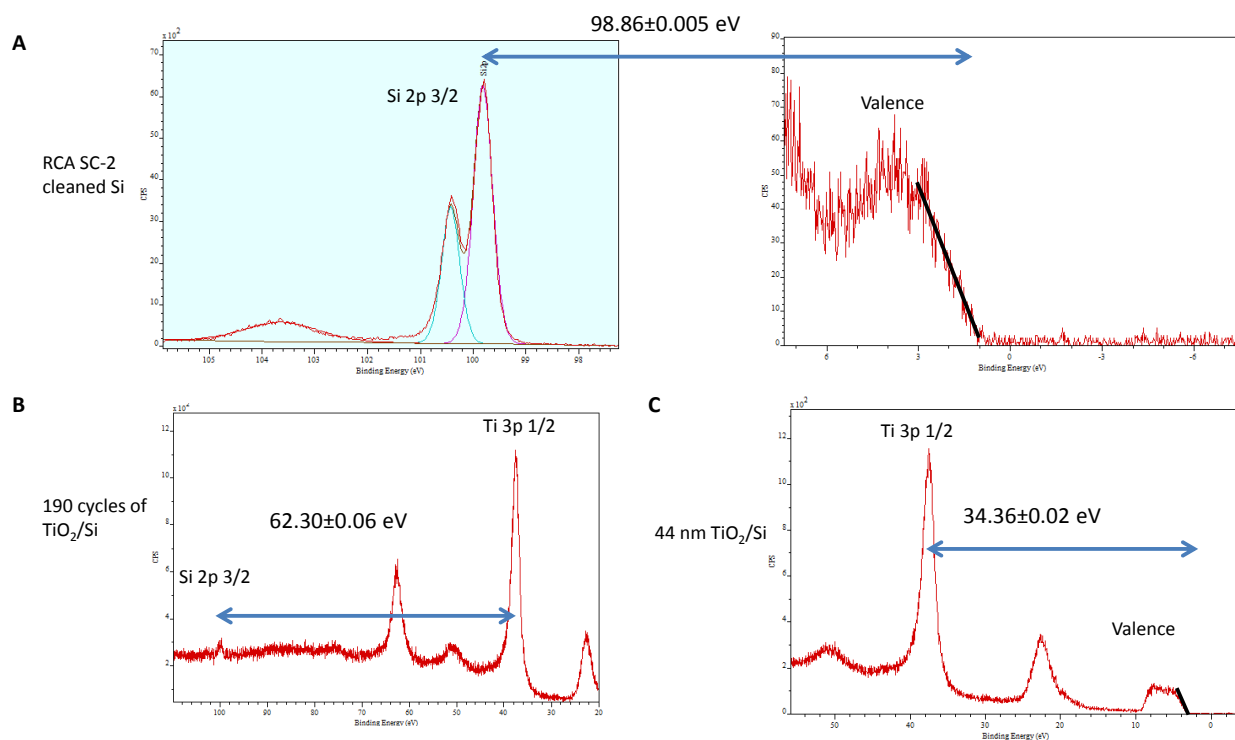


Fig. S13.

X-ray photoelectron spectroscopy showing core-level spectra for Ti and Si, as well as the valence-band spectra. High-resolution scan of the Si 2p core-level spectra and the valence-band spectra of RCA SC-2 cleaned Si (A); Si 2p and Ti 3p core-level spectra of 190 ALD cycles of TiO_2 on Si (B); and Ti 3p core-level spectra and valence-band spectra of 44 nm unannealed TiO_2 on Si.

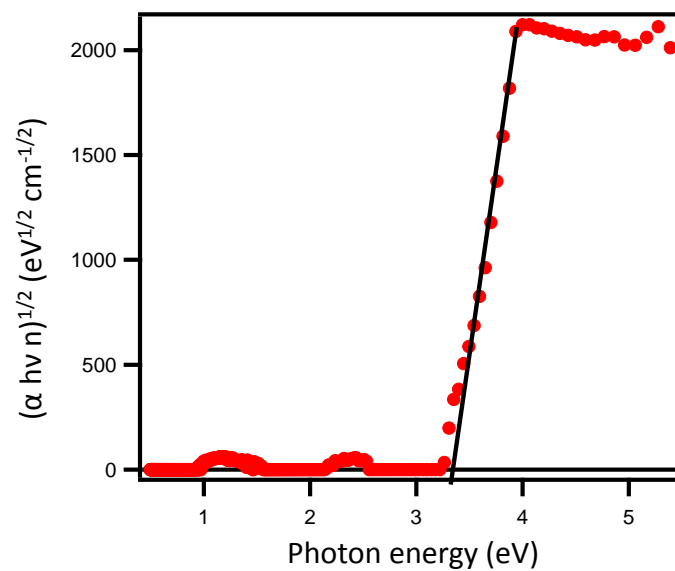


Fig. S14.

Tauc plot of ALD-grown TiO₂ based on its energy-dependent complex refractive indices (n , k). The intersection with the horizontal axis indicates a direct optical gap of 3.34 ± 0.01 eV.

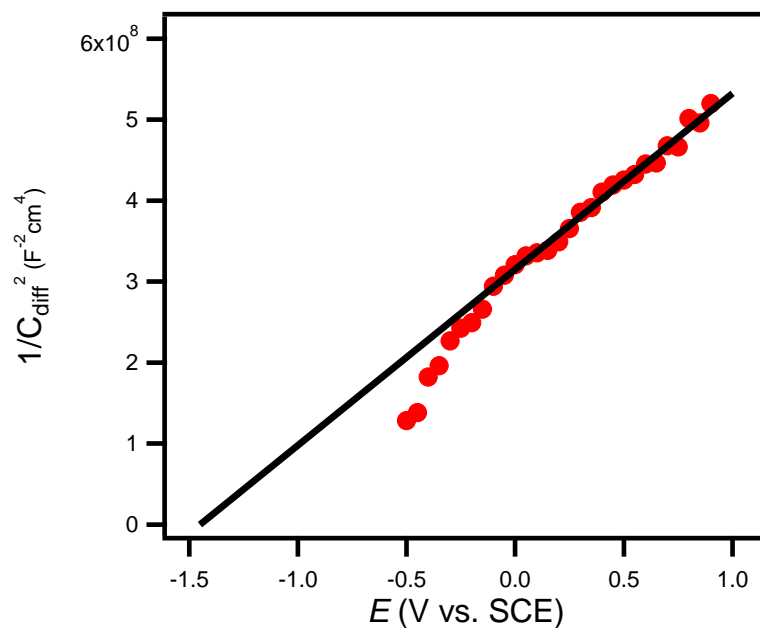


Fig. S15.

Mott-Schottky analysis of the inverse square of the differential capacitance (C_{diff}) vs potential (E) of an ALD-deposited 143 nm thick TiO_2 film on $\text{n}^+\text{-Si}$ in contact with 50 mM $\text{K}_3\text{Fe(CN)}_6$ and 350 mM of $\text{K}_4\text{Fe(CN)}_6$ in H_2O . The analysis was performed using electrochemical impedance spectroscopy.

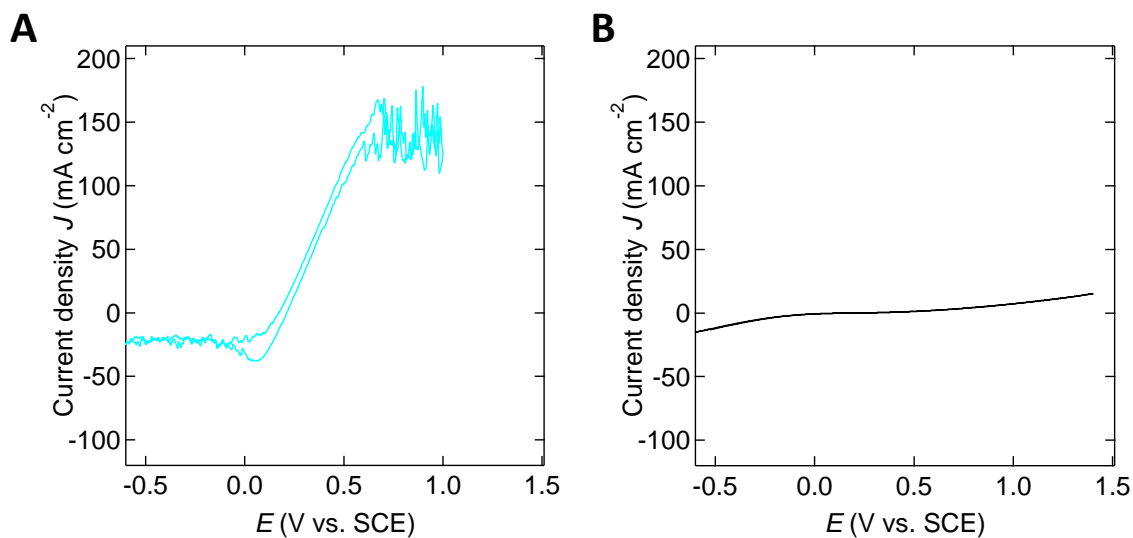


Fig. S16.

Dark J - E behavior of a nominally 100 nm Ni film on a 4 nm ALD-TiO₂ film on p⁺-Si in contact with 50 mM K₃Fe(CN)₆ and 350 mM K₄Fe(CN)₆ in H₂O, without (A) and with (B) the ALD-TiO₂ film annealed at 450 °C for 2 h. The Ni film was deposited after the annealing. The conductivity through the 4 nm TiO₂ film decreased significantly after the film was annealed.

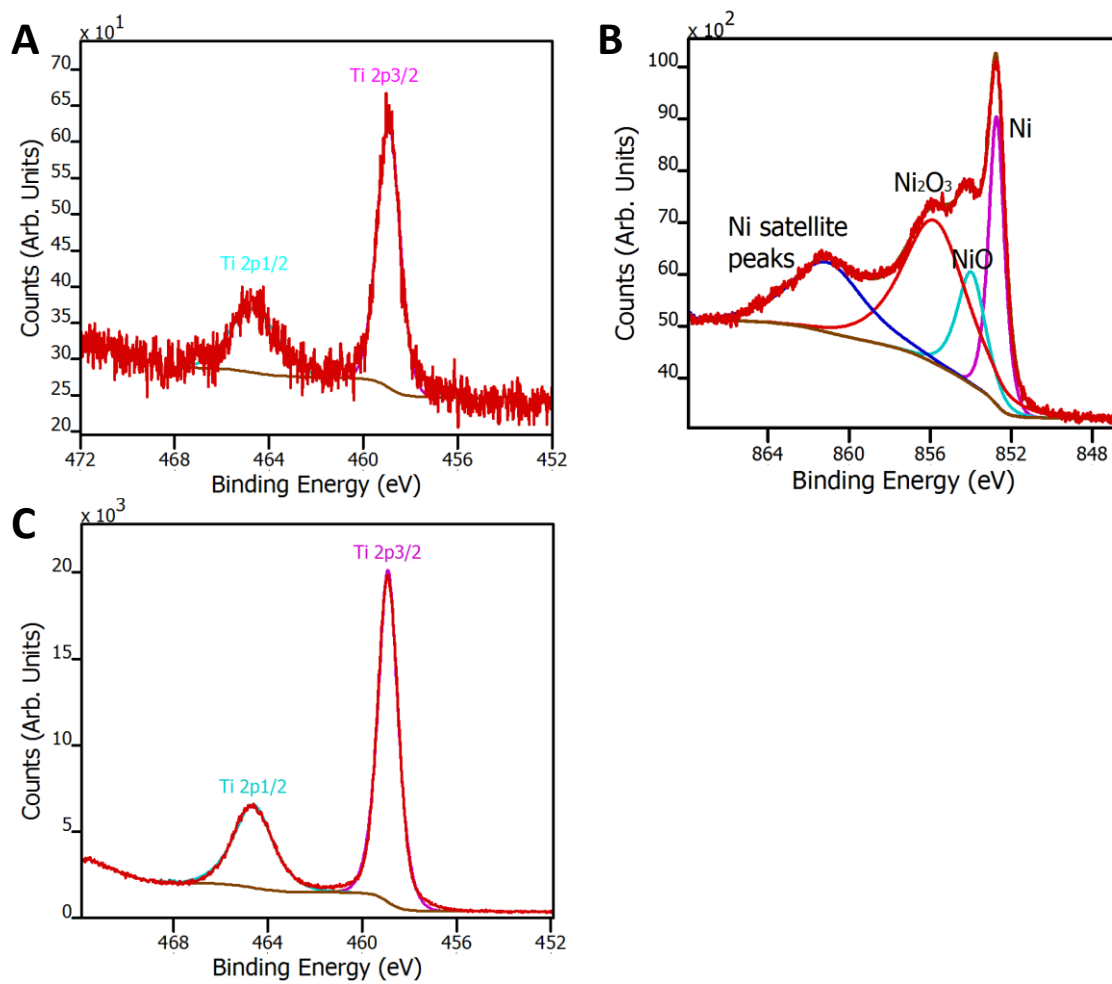


Fig. S17.

X-ray photoelectron spectroscopy of the Ti 2p (A) and Ni 2p (B) core levels for the surface of 3 nm Ni on TiO₂, as well as the Ti 2p (C) for the surface of as-grown TiO₂.

References and Notes

1. N. Lewis, An integrated, systems approach to the development of solar fuel generators. *Electrochem. Soc. Interface* **22**, 43–49 (2013).
2. B. A. Pinaud, J. D. Benck, L. C. Seitz, A. J. Forman, Z. Chen, T. G. Deutsch, B. D. James, K. N. Baum, G. N. Baum, S. Ardo, H. Wang, E. Miller, T. F. Jaramillo, Technical and economic feasibility of centralized facilities for solar hydrogen production via photocatalysis and photoelectrochemistry. *Energy Environ. Sci.* **6**, 1983–2002 (2013). [doi:10.1039/c3ee40831k](https://doi.org/10.1039/c3ee40831k)
3. M. G. Walter, E. L. Warren, J. R. McKone, S. W. Boettcher, Q. Mi, E. A. Santori, N. S. Lewis, Solar water splitting cells. *Chem. Rev.* **110**, 6446–6473 (2010). [doi:10.1021/cr1002326](https://doi.org/10.1021/cr1002326) [Medline](#)
4. M. Pourbaix, *Atlas of Electrochemical Equilibria in Aqueous Solutions* (National Association of Corrosion Engineers, Houston, TX, ed. 2, 1974).
5. J. R. McKone, N. S. Lewis, H. B. Gray, Will solar-driven water-splitting devices see the light of day? *Chem. Mater.* **26**, 407–414 (2014). [doi:10.1021/cm4021518](https://doi.org/10.1021/cm4021518)
6. S. Hu, C. Xiang, S. Haussener, A. D. Berger, N. S. Lewis, An analysis of the optimal band gaps of light absorbers in integrated tandem photoelectrochemical water-splitting systems. *Energy Environ. Sci.* **6**, 2984–2993 (2013). [doi:10.1039/c3ee40453f](https://doi.org/10.1039/c3ee40453f)
7. Y. Nakato, T. Ohnishi, H. Tsubomura, Photo-electrochemical behaviors of semiconductor electrodes coated with thin metal films. *Chem. Lett.* **3**, 883–886 (1975). [doi:10.1246/cl.1975.883](https://doi.org/10.1246/cl.1975.883)
8. R. C. Kainthla, Significant efficiency increase in self-driven photoelectrochemical cell for water photoelectrolysis. *J. Electrochem. Soc.* **134**, 841–845 (1987). [doi:10.1149/1.2100583](https://doi.org/10.1149/1.2100583)
9. M. J. Kenney, M. Gong, Y. Li, J. Z. Wu, J. Feng, M. Lanza, H. Dai, High-performance silicon photoanodes passivated with ultrathin nickel films for water oxidation. *Science* **342**, 836–840 (2013). [doi:10.1126/science.1241327](https://doi.org/10.1126/science.1241327) [Medline](#)
10. F. R. F. Fan, R. G. Keil, A. J. Bard, Semiconductor electrodes. 48. Photooxidation of halides and water on n-silicon protected with silicide layers. *J. Am. Chem. Soc.* **105**, 220–224 (1983). [doi:10.1021/ja00340a013](https://doi.org/10.1021/ja00340a013)
11. F. Decker, M. Fracastoro-Decker, W. Badawy, K. Doblhofer, H. Gerischer, The photocurrent-voltage characteristics of the heterojunction combination n-Si/SnO₂/redox-electrolyte. *J. Electrochem. Soc.* **130**, 2173–2179 (1983). [doi:10.1149/1.2119547](https://doi.org/10.1149/1.2119547)
12. F. Fan, B. Wheeler, A. Bard, R. Noufi, Semiconductor electrodes XXXIX. Techniques for stabilization of n-silicon electrodes in aqueous solution photoelectrochemical cells. *J. Electrochem. Soc.* **128**, 2042–2045 (1981). [doi:10.1149/1.2127794](https://doi.org/10.1149/1.2127794)
13. N. C. Strandwitz, D. J. Comstock, R. L. Grimm, A. C. Nichols-Nieler, J. Elam, N. S. Lewis, Photoelectrochemical behavior of n-type Si(100) electrodes coated with thin films of manganese oxide grown by atomic layer deposition. *J. Phys. Chem. C* **117**, 4931–4936 (2013). [doi:10.1021/jp311207x](https://doi.org/10.1021/jp311207x)

14. K. Sun, N. Park, Z. Sun, J. Zhou, J. Wang, X. Pang, S. Shen, S. Y. Noh, Y. Jing, S. Jin, P. K. L. Yu, D. Wang, Nickel oxide functionalized silicon for efficient photo-oxidation of water. *Energy Environ. Sci.* **5**, 7872–7877 (2012). [doi:10.1039/c2ee21708b](https://doi.org/10.1039/c2ee21708b)
15. Y. W. Chen, J. D. Prange, S. Dühnen, Y. Park, M. Gunji, C. E. Chidsey, P. C. McIntyre, Atomic layer-deposited tunnel oxide stabilizes silicon photoanodes for water oxidation. *Nat. Mater.* **10**, 539–544 (2011). [doi:10.1038/nmat3047](https://doi.org/10.1038/nmat3047) [Medline](#)
16. A. G. Scheuermann, J. D. Prange, M. Gunji, C. E. D. Chidsey, P. C. McIntyre, Effects of catalyst material and atomic layer deposited TiO₂ oxide thickness on the water oxidation performance of metal–insulator–silicon anodes. *Energy Environ. Sci.* **6**, 2487–2496 (2013). [doi:10.1039/c3ee41178h](https://doi.org/10.1039/c3ee41178h)
17. S. Dueñas, H. Castán, H. García, E. S. Andrés, M. Toledano-Luque, I. Mártel, G. González-Díaz, K. Kukli, T. Uustare, J. Aarik, A comparative study of the electrical properties of TiO₂ films grown by high-pressure reactive sputtering and atomic layer deposition. *Semicond. Sci. Technol.* **20**, 1044–1051 (2005). [doi:10.1088/0268-1242/20/10/011](https://doi.org/10.1088/0268-1242/20/10/011)
18. Materials and methods are available as supplementary materials on *Science Online*.
19. Y. Matsumoto, E. Sato, Electrocatalytic properties of transition metal oxides for oxygen evolution reaction. *Mater. Chem. Phys.* **14**, 397–426 (1986). [doi:10.1016/0254-0584\(86\)90045-3](https://doi.org/10.1016/0254-0584(86)90045-3)
20. D. A. Corrigan, Effect of coprecipitated metal ions on the electrochemistry of nickel hydroxide thin films: Cyclic voltammetry in 1M KOH. *J. Electrochem. Soc.* **136**, 723–728 (1989). [doi:10.1149/1.2096717](https://doi.org/10.1149/1.2096717)
21. B. S. Yeo, A. T. Bell, In situ raman study of nickel oxide and gold-supported nickel oxide catalysts for the electrochemical evolution of oxygen. *J. Phys. Chem. C* **116**, 8394–8400 (2012). [doi:10.1021/jp3007415](https://doi.org/10.1021/jp3007415)
22. H. N. Ghosh, J. B. Asbury, Y. Weng, T. Lian, Interfacial electron transfer between Fe(II)(CN)₆⁴⁻ and TiO₂ nanoparticles: Direct electron injection and nonexponential recombination. *J. Phys. Chem. B* **102**, 10208–10215 (1998). [doi:10.1021/jp983502w](https://doi.org/10.1021/jp983502w)
23. S. A. Campbell, H.-S. Kim, D. C. Gilmer, B. He, T. Ma, W. L. Gladfelter, Titanium dioxide (TiO₂)-based gate insulators. *IBM J. Res. Develop.* **43**, 383–392 (1999). [doi:10.1147/rd.433.0383](https://doi.org/10.1147/rd.433.0383)
24. B. Kalanyan, G. Parsons, Atomic layer deposited oxides for passivation of silicon photoelectrodes for solar photoelectrochemical cells. *ECS Trans.* **41**, 285–292 (2011).
25. M. H. Lee, K. Takei, J. Zhang, R. Kapadia, M. Zheng, Y. Z. Chen, J. Nah, T. S. Matthews, Y. L. Chueh, J. W. Ager, A. Javey, p-Type InP nanopillar photocathodes for efficient solar-driven hydrogen production. *Angew. Chem. Int. Ed. Engl.* **51**, 10760–10764 (2012). [doi:10.1002/anie.201203174](https://doi.org/10.1002/anie.201203174) [Medline](#)
26. A. Paracchino, V. Laporte, K. Sivula, M. Grätzel, E. Thimsen, Highly active oxide photocathode for photoelectrochemical water reduction. *Nat. Mater.* **10**, 456–461 (2011). [doi:10.1038/nmat3017](https://doi.org/10.1038/nmat3017) [Medline](#)

27. B. Seger, T. Pedersen, A. B. Laursen, P. C. Vesborg, O. Hansen, I. Chorkendorff, Using TiO₂ as a conductive protective layer for photocathodic H₂ evolution. *J. Am. Chem. Soc.* **135**, 1057–1064 (2013). [doi:10.1021/ja309523t](https://doi.org/10.1021/ja309523t) [Medline](#)
28. S. Avasthi, W. E. McClain, G. Man, A. Kahn, J. Schwartz, J. C. Sturm, Hole-blocking titanium-oxide/silicon heterojunction and its application to photovoltaics. *Appl. Phys. Lett.* **102**, 203901 (2013). [doi:10.1063/1.4803446](https://doi.org/10.1063/1.4803446)
29. C. C. L. McCrory, S. Jung, J. C. Peters, T. F. Jaramillo, Benchmarking heterogeneous electrocatalysts for the oxygen evolution reaction. *J. Am. Chem. Soc.* **135**, 16977–16987 (2013). [doi:10.1021/ja407115p](https://doi.org/10.1021/ja407115p) [Medline](#)
30. M. R. Shaner, K. T. Fountaine, H.-J. Lewerenz, Current-voltage characteristics of coupled photodiode-electrocatalyst devices. *Appl. Phys. Lett.* **103**, 143905 (2013). [doi:10.1063/1.4822179](https://doi.org/10.1063/1.4822179)
31. R. L. Grimm, M. J. Bierman, L. E. O’Leary, N. C. Strandwitz, B. S. Brunschwig, N. S. Lewis, Comparison of the photoelectrochemical behavior of H-terminated and methyl-terminated Si(111) surfaces in contact with a series of one-electron, outer-sphere redox couples in CH₃CN. *J. Phys. Chem. C* **116**, 23569–23576 (2012). [doi:10.1021/jp308461q](https://doi.org/10.1021/jp308461q)
32. J. Mukherjee, S. Peczonczyk, S. Maldonado, Wet chemical functionalization of III-V semiconductor surfaces: Alkylation of gallium phosphide using a Grignard reaction sequence. *Langmuir* **26**, 10890–10896 (2010). [doi:10.1021/la100783w](https://doi.org/10.1021/la100783w) [Medline](#)
33. M. Perego, G. Seguni, G. Scarel, M. Fanciulli, F. Wallrapp, Energy band alignment at TiO₂/Si interface with various interlayers. *J. Appl. Phys.* **103**, 043509 (2008). [doi:10.1063/1.2885109](https://doi.org/10.1063/1.2885109)